THE JOURNAL OF PHYSICAL CHEMISTRY A
A JOURNAL OF THE AMERICAN CHEMICAL SOCIETY

pubs.acs.org/JPCA

Article

Experimental and Theoretical Study of Oxolan-3-one Thermal Decomposition

Heather N. Legg, Kathryn M. Narkin, Laura R. McCunn,* Carol A. Parish, and Xinli Song*

Cite This: *J. Phys. Chem. A* 2022, 126, 7084−7093

Read Online

ACCESS | Metrics & More | Article Recommendations | Supporting Information

ABSTRACT: The thermal decomposition of oxolan-3-one, a common component of the bio-oil formed during biomass pyrolysis, has been studied using *ab initio* calculations and experiments employing pulsed gas-phase pyrolysis with matrix-isolation FTIR product detection. Four pathways for unimolecular decomposition were predicted using computational methods. The dominant reaction channel led to carbon monoxide, formaldehyde, and ethylene, all of which were observed experimentally. The other channels led to an assortment of products including ketene, water, propyne, and acetylene, which were all confirmed in the matrix-isolation FTIR spectra. There is also evidence for the production of substituted ketenes in pyrolysis, most likely hydroxyketene and methylketene.

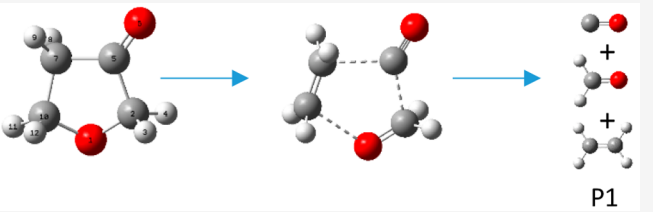

INTRODUCTION

Biofuels generated from biomass have the potential to meet a significant portion of the world's energy needs and reduce the reliance on fossil fuels. Biomass can be processed into biofuels via a microbial-mediated transformation or thermochemical conversion. Pyrolysis, gasification, and hydrothermal liquefaction are all thermochemical conversion techniques; however, much research has focused on pyrolysis, as it is considered the most economical and environmentally sustainable.[1] The pyrolysis of lignocellulosic biomass from various plant feedstocks breaks down structural biopolymers including cellulose, lignin, and hemicelluloses[1] and leads to gases, biochars, and bio-oils[2] that can be refined into usable fuel.[3,4] Bio-oil is a complex mixture of water, hydrocarbons, aromatics, oxygenated hydrocarbons, and nitrogen-containing compounds.[1,5−7] In order to understand the chemistry and environmental impact of the pyrolytic generation of bio-oil, the refining of bio-oil, and the combustion of the final biofuel product, it is imperative to determine the mechanisms of thermal decomposition for all components of bio-oil.

One common bio-oil component is oxolan-3-one, a cyclic oxygenated hydrocarbon with the chemical formula $C_4H_6O_2$ (Scheme 1). It is found in the pyrolysis products of many types of wood and fungal rotted wood.[8,9] Pyrolysis experiments on wood performed by Galletti et al. using gas chromatography and mass spectrometry revealed oxolan-3-one was one of many pyrolysis products derived from lignin and polysaccharides.[10] Pyrolysis mass spectrometry studies by Mulder et al. showed how rot altered wood, causing a molecular change in the lignin and affecting the composition of the bio-oil that included oxolan-3-one.[11] The use of wood chips and wood pellets for fuel generation has been increasing and will continue to increase in coming years, making oxolan-3-one an important compound to study.[8] Although the occurrence of oxolan-3-one in the pyrolysis of wood is well established, there is no study of how oxolan-3-one can undergo subsequent reactions at high temperatures or how those products may impact the composition, efficiency, and emissions of a biofuel.

The purpose of this work is to understand the thermal decomposition mechanism of oxolan-3-one. Pyrolysis is accomplished in the gas phase with a pulsed microtubular reactor,[12] and the products are identified by matrix-isolation FTIR. The relatively short residence time in the reactor (∼100 μs), followed by rapid cooling in a supersonic expansion and freezing in an argon matrix, allows the detection of products, even intermediates, from early steps in the pyrolysis mechanism. The results are compared to computational predictions in an effort to develop a mechanism for oxolan-3-one pyrolysis.

EXPERIMENTAL METHODS

A gas-phase mixture of oxolan-3-one (0.1%−0.4%) in argon was prepared with a total pressure of approximately 950 Torr using standard manometric techniques. The oxolan-3-one (>98.0% purity) was purchased from TCI America and used without further purification. The mixture was then expanded through the 0.1 mm diameter orifice of a pulsed valve (Parker General Valve Series 9) into a silicon carbide (SiC) tube with a

Received: May 10, 2022
Revised: September 21, 2022
Published: October 4, 2022

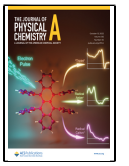

Scheme 1. Pyrolysis Pathways for Oxolan-3-one

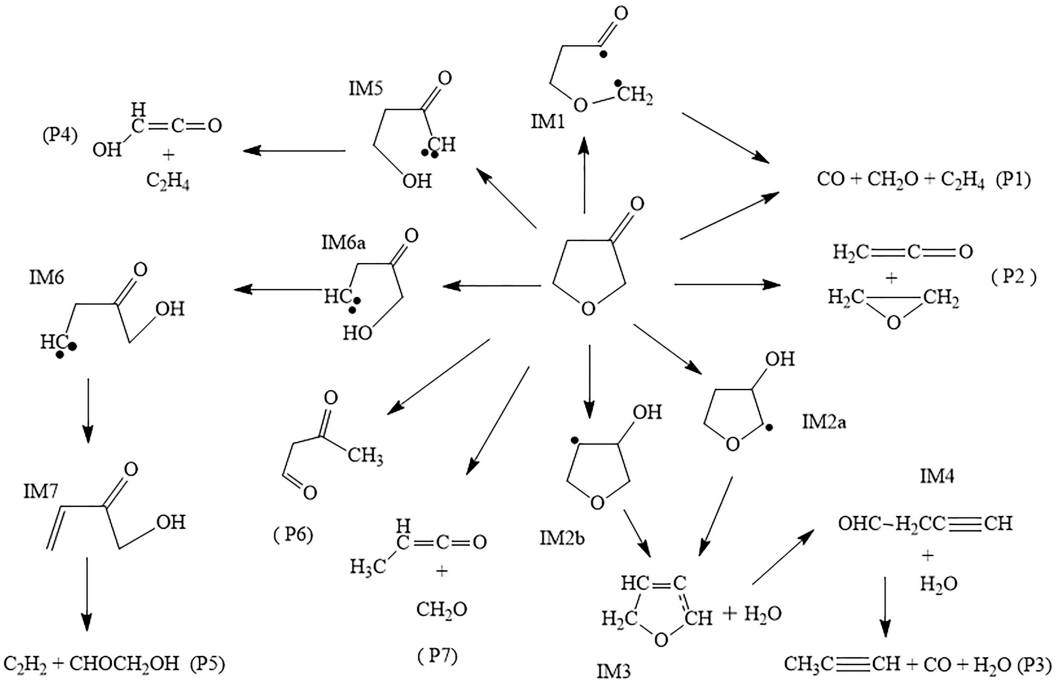

1.0 mm inner diameter and 38.1 mm length. The SiC tube was resistively heated by a variable transformer to temperatures ranging from 800 to 1400 K; the temperature was measured by a type C thermocouple mounted to the outside of the tube. Then, the products of pyrolysis were jetted onto the cesium iodide (CsI) window mounted in a rotatable-shroud cryostat (Janis Research), with a typical pressure of 1×10^{-6} Torr. The CsI window was cooled by a closed-cycle helium compressor (Sumitomo Heavy Industries CAN-11) and maintained at 15 K by a Lake Shore 331 temperature controller during deposition to freeze the pyrolysis products in an argon matrix. Deposition was accomplished with a pulsed valve on-time of 200 μs and an off-time of 20 ms, resulting in a deposition rate of 5−6 mmol/hour. Following 3 h of deposition, the CsI window was cooled from 15 to 4 K. Then, 128 scans were recorded by a Bruker Vertex 70 Fourier-transform infrared spectrometer (FTIR) with a dry air purge and a 0.5 cm^{-1} resolution. The resultant spectra were analyzed to determine the products of the oxolan-3-one pyrolysis. Control experiments were performed by depositing an oxolan-3-one/argon mixture on the silicon carbide tube held at room temperature.

COMPUTATIONAL METHODS

All *ab initio* calculations were carried out using the Gaussian 16 program.[13] For computational efficiency, the geometries of all possible stationary points (e.g., reactants, products, intermediates, and transition states) were optimized at the B3LYP/6-311G(2d, d, p) level of theory.[14] Local minima and transition states were confirmed to have all real frequencies and only one imaginary frequency, respectively. Animation of the imaginary vibrational modes in combination with the intrinsic reaction coordinate (IRC)[15] confirmed that the transition states connected the reactants with the corresponding products.

The relative energies for the pyrolysis reaction of oxolan-3-one were re-evaluated using the CBS-QB3[16] and G4MP2[17] methods, respectively. The CBS-QB3 scheme uses the B3LYP/CBSB7-optimized geometrical parameters and zero-point energies (ZPEs). The CBSB7 basis set is equivalent to the 6-311G(2d, d, p) basis set. For comparison, G4MP2 energies were calculated using the same geometries and ZPEs. These two composite approaches were previously employed to generate energetic profiles for similar reactions with chemical accuracy.[18,19] The dependence of the geometrical parameters on the level of theory was examined using the MP2/6-311++G(d, p) method for some key stationary points. The deviations between the CBS-QB3 and G4MP2 geometries are marginal.

RESULTS AND DISCUSSION

In total, 12 product channels have been studied for the pyrolysis of oxolan-3-one, as shown in R1−R12 and Scheme 1.

$$C_4H_6O_2 \rightarrow CO + CH_2O + C_2H_4 \quad \text{(ethylene)} \tag{R1}$$

$$CH_2CO\ \text{(ketene)} + \text{cyc-}CH_2OCH_2 \quad \text{(ethylene oxide)} \tag{R2}$$

$$CO + H_2O + CH_3CCH \quad \text{(propyne)} \tag{R3}$$

$$C_2H_4 + HOCHCO \quad \text{(hydroxyketene)} \tag{R4}$$

$$HOCH_2CHO + C_2H_2 \quad \text{(acetylene)} \tag{R5}$$

$$CH_3C(O)CH_2CHO \quad (\text{linear } C_4H_6O_2) \tag{R6}$$

$$CH_2O + CH_3CHCO \quad \text{(methylketene)} \tag{R7}$$

$$CH_2CH_2OCH_2C(O)\bullet \quad \text{(C−C rupture)} \tag{R8}$$

$$CH_2OCH_2C(O)CH_2\bullet \quad \text{(C−C rupture)} \tag{R9}$$

$$CH_2OCH_2CH_2C(O)\bullet \quad \text{(C−C rupture)} \tag{R10}$$

https://doi.org/10.1021/acs.jpca.2c03254
J. Phys. Chem. A 2022, 126, 7084−7093

$OCH_2CH_2C(O)CH_2\bullet$ (C−O rupture) (R11)

$CH_2CH_2C(O)CH_2O\bullet$ (C−O rupture) (R12)

In most cases, the MP2 geometries are very similar to the B3LYP/CBSB7 geometries. In only one case do we see a difference in optimized geometries (Table 1, TS3). The uncertainties of the energies can be estimated from the data in Table 1, which were calculated at different levels of theory. Considering the good performance of CBS-QB3 for these systems, the CBS-QB3 geometries and energies are used in the following discussions unless stated otherwise.

Table 1. Relative Energies (kcal/mol) for the Pyrolysis Reaction of Oxolan-3-one

species	CBS-QB3	G4MP2	MP2/6-311++G(d,p)
R	0.00	0.00	0.00
TS1	57.86	54.75	53.44
TS2	87.24	82.74	90.26
TS3	87.64	80.26	86.89[a]
TS4	90.96	85.60	85.59
TS5a	77.69	76.12	75.74
TS5b	74.76	71.72	72.43
TS6a	114.44	108.04	110.99
TS6b	118.84	112.66	115.58
TS7 + H_2O	96.47	90.49	90.60
TS8 + H_2O	107.87	100.37	97.53
TS9	73.61	70.42	71.08
TS10	73.39	69.78	71.02
TS11	79.11	79.46	81.48
TS12	80.64	79.73	82.20
TS13	99.44	97.90	99.23
TS14	79.89	74.78	88.86
TS15	96.31	92.43	93.01
IM1	64.63	58.20	52.81[a]
IM2a	13.98	13.05	14.73
IM2b	12.25	11.45	13.55
IM3 + H_2O	71.75	66.80	67.83
IM4 + H_2O	33.51	30.06	27.65
IM5	65.63	62.25	63.54
IM6	79.98	78.14	82.54
IM7	4.80	3.78	4.98
P1 ($CO + CH_2O + C_2H_4$)	26.03	21.34	21.54
P2 ($CH_2CO + CH_2OCH_2$)	43.39	40.76	41.02
P3 ($H_2O + CH_3CCH + CO$)	27.10	22.23	20.88
P4 (C_2H_4 + HOCHCO)	44.15	40.84	42.68
P5 ($CHOCH_2OH + C_2H_2$)	46.71	43.53	43.20
P6 (CH_3COCH_2CHO)	−5.39	−7.23	−7.98
P7 ($CH_2O + CH_3CHCO$)	25.63	23.31	21.94

[a]The MP2-optimized geometries for TS3 and IM1 are different from those optimized at the CBS-QB3 level.

A. PATH I: THE PATHWAY FOR FORMATION OF P1 (CARBON MONOXIDE, FORMALDEHYDE, AND ETHYLENE) (R1)

This pathway undergoes the simultaneous rupture of two C−C bonds and one C−O bond via transition state TS1 (Figure 1). In the transition state, the three rupturing bonds are elongated by 0.4−0.8 Å. TS1 is calculated to be 57.86 kcal/mol above oxolan-3-one. This concerted process leads to CO + CH_2O + C_2H_4 products (P1), which are 26.03 kcal/mol higher in energy than the oxolan-3-one reactant. (Figure 2)

The experimental results are consistent with the products of path I. Carbon monoxide was observed as a product at 2139 cm^{-1} (Figure 3), at 2091 cm^{-1} as the ^{13}CO isotopomer, and also at 2149 cm^{-1} in a complex of $CO{\cdot}H_2O$.[20−23] While CO is a common contaminant from the heated silicon carbide tube, there is evidence that most of the CO observed in these experiments indeed comes from the pyrolysis of oxolan-3-one. The integrated absorbance for the peak at 2139 cm^{-1} was determined for both the spectrum collected following the pyrolysis of oxolan-3-one at 1300 K and the spectrum collected following the heating of pure argon under the same conditions. The pyrolysis of oxolan-3-one resulted in approximately 50× greater absorbance for the CO band than did the heating of pure argon. As shown in Figures 4−8, formaldehyde bands[24−27] are present at the wavenumbers 3465, 2865, 2797, 2719, 1742, 1498, 1245, and 1169 cm^{-1}. As shown in Figures 4−8, ethylene is evidenced[28−30] by peaks at 3111, 3081, 3071, 2995, 1440, and 946 cm^{-1}.

B. PATH II: THE PATHWAY FOR THE FORMATION OF P1 (R1) AND P2 (ETHYLENE OXIDE AND KETENE, R2)

This pathway has two subpathways initiated by the fission of either one or two C−C bonds. In the first subpathway, oxolan-3-one undergoes bond rupture at C2−C5 (atom numbering shown in Figure 1), providing an alternate route to CO + CH_2O + C_2H_4 (P1). The transition state for this process is TS2, where the C2−C5 bond is elongated from 1.532 to 2.852 Å. TS2 (Figure 9) leads to the linear intermediate IM1 (Figure S1). IM1 further decomposes via the concerted transition state TS3 (Figure 9) to form the three products CO, CH_2O, and C_2H_4 (P1). In TS3, both C−C and C−O bonds break apart

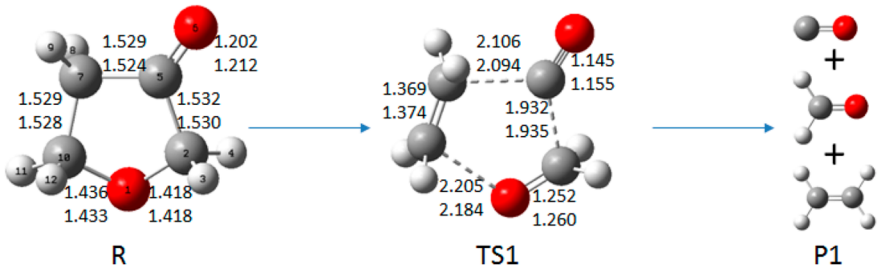

Figure 1. Optimized geometries (Å) of species involved in the simultaneous rupture of two C−C bonds and one C−O bond in oxolan-3one (top, B3LYP/CBSB7; bottom, MP2/6-311++G**).

https://doi.org/10.1021/acs.jpca.2c03254
J. Phys. Chem. A 2022, 126, 7084−7093

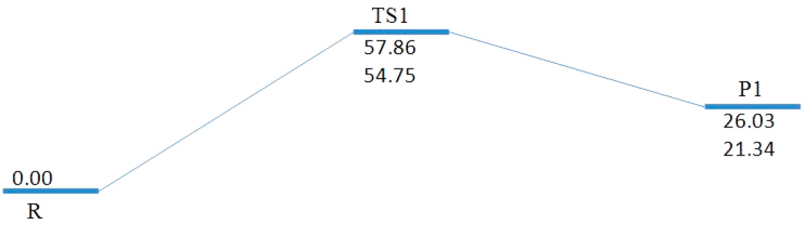

Figure 2. Relative energies (kcal/mol) of species involved in path I (top, CBS-QB3; bottom, G4MP2.).

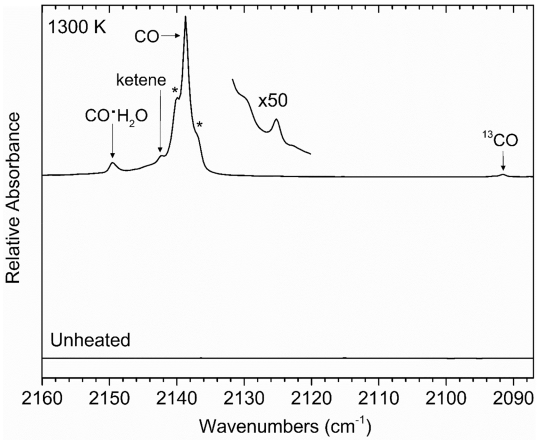

Figure 3. Comparison of the matrix-isolation FTIR spectrum collected after the pyrolysis of 0.4% oxolan-3-one in argon at 1300 K and the spectrum of the unheated sample. Note that the *y*-axis has a much larger range than other spectra in this paper due to carbon monoxide's large absorbance relative to other products. The bands marked with asterisks are suspected to belong to substituted ketenes. The 2132−2120 cm^{-1} region is magnified 50× to show detail.

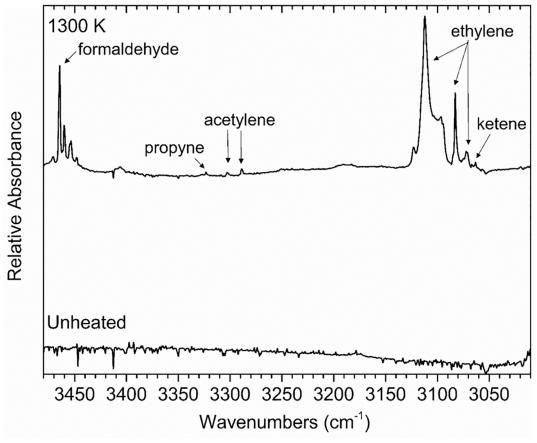

Figure 4. Comparison of the matrix-isolation FTIR spectrum collected after the pyrolysis of 0.4% oxolan-3-one in argon at 1300 K and the spectrum of the unheated sample.

simultaneously. It is noted that the geometry of TS3 on the MP2/6-311++G** surface is different from the geometry on the B3LYP/CBSB7 surface (Figure S1). This is not surprising given the conformational flexibility of this structure.

The second subpathway has C2−C5 and C7−C10 dissociating simultaneously via TS4 (Figure 9) to form ketene and ethylene oxide (Figure S1). In TS4, the C7−C10 bond is elongated to 3.129 Å, and the C2−C5 bond is stretched to 2.212 Å. Clearly, TS4 is a late transition state that is very close in geometry to the final product P2 (ethylene oxide + ketene).

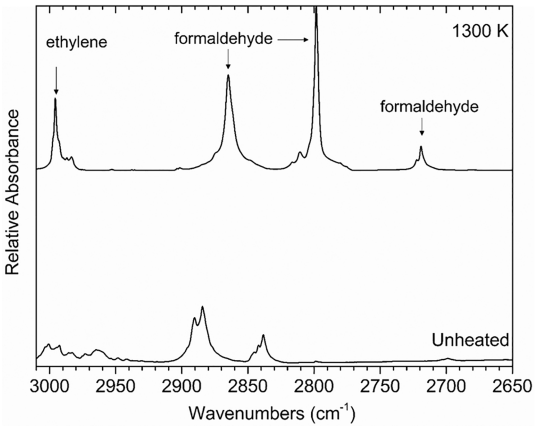

Figure 5. Comparison of the matrix-isolation FTIR spectrum collected after the pyrolysis of 0.4% oxolan-3-one in argon at 1300 K and the spectrum of the unheated sample.

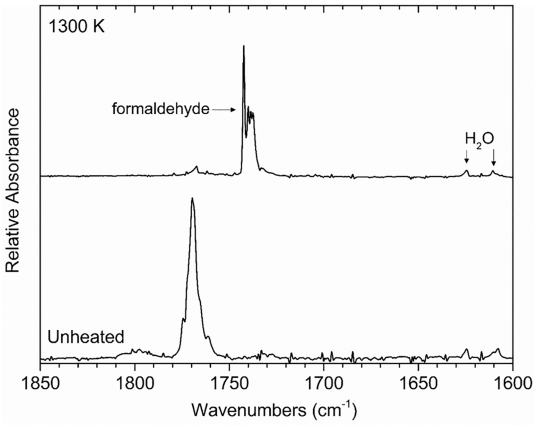

Figure 6. Comparison of the matrix-isolation FTIR spectrum collected after the pyrolysis of 0.4% oxolan-3-one in argon at 1300 K and the spectrum of the unheated sample.

The calculated barrier height of TS4 is 90.96 kcal/mol, which is only about 3 kcal/mol higher than that of TS2, suggesting that these pathways have similar kinetic probabilities. Energetically, path II is more likely to produce P1, as P2 is significantly more endothermic than P1 (Figure 10).

In the experimental spectra collected following the pyrolysis of oxolan-3-one, three vibrational bands of ketene can be seen in Figures 3, 4, and 7, at 2142, 3063, and 1380 cm^{-1}, in accordance with the literature.[31−33] Ethylene oxide was not observed in the infrared spectra, but it is known that ethylene oxide can isomerize to form acetaldehyde. Acetaldehyde can decompose at the temperatures employed in these experiments into CO + CH_3 + H, ketene + H_2, and HCCH + H_2O.[34] It should be noted that CO and ketene had already been

https://doi.org/10.1021/acs.jpca.2c03254
J. Phys. Chem. A 2022, 126, 7084−7093

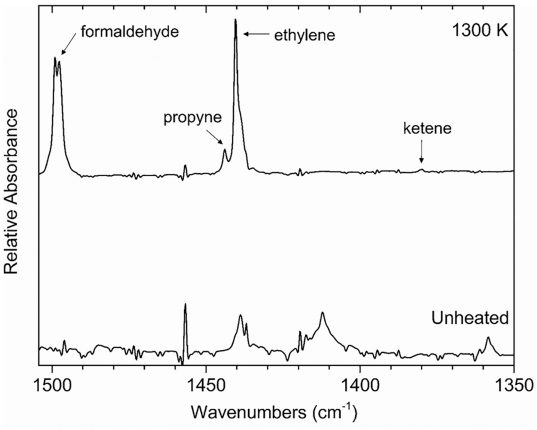

Figure 7. Comparison of the matrix-isolation FTIR spectrum collected after the pyrolysis of 0.4% oxolan-3-one in argon at 1300 K and the spectrum of the unheated sample.

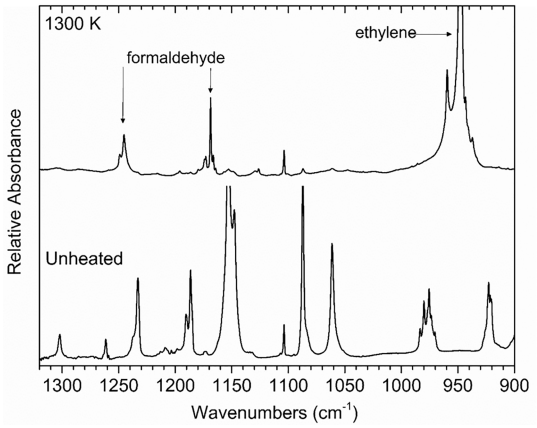

Figure 8. Comparison of the matrix-isolation FTIR spectrum collected after the pyrolysis of 0.4% oxolan-3-one in argon at 1300 K and the spectrum of the unheated sample.

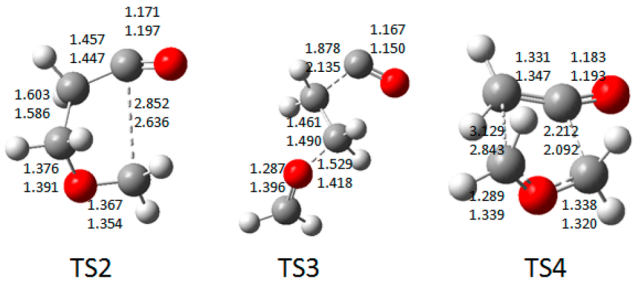

Figure 9. Optimized transition state geometries (Å) involved in path II (top, B3LYP/CBSB7; bottom, MP2/6-311++G**).

observed in these experiments. Additionally, acetylene can be found at 3302 and 3288 cm^{-1} in Figure 4, consistent with bands reported in the literature.[31,35−37] It is possible that ethylene oxide has undergone secondary reactions and thus diluted the FTIR absorbance, although stable ethylene oxide has been observed in the pyrolysis of 3-oxetanone under similar conditions.[38]

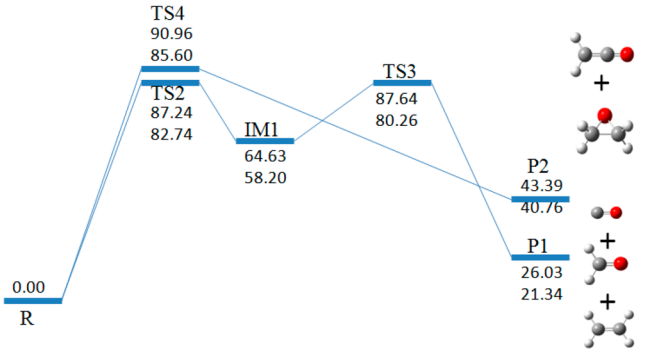

Figure 10. Relative energies (kcal/mol) of species involved in path II (top, CBS-QB3; bottom, G4MP2).

C. PATH III: THE PATHWAY FOR FORMATION OF P3 (CO + H_2O + PROPYNE, R3)

This pathway is initiated by hydrogen migration from the methylene groups on either side of the carbonyl moiety to the carbonyl oxygen atom. A H atom shift from C2 occurs via TS5a, while H atom migration from C7 occurs via TS5b (Figure 11). Both TS5a and TS5b are four-membered cyclic transition states. The barrier height of TS5a is approximately 3 kcal/mol higher than that of TS5b, as seen in Figure 12. TS5a and TS5b lead to the corresponding hydroxy intermediates IM2a and IM2b (Figure S2). For both channels, these intermediates can undergo a second H migration via another four-membered cyclic transition state (TS6a and TS6b) to form intermediate IM3 (C_4H_4O) by the elimination of H_2O. IM3 appears to be an aromatic singlet carbene, with a lone pair of electrons on C5 (see atom numbering in Figure 1; additional structural details as shown in Figure S3). IM3 undergoes further H shifting and C−O bond fission via TS7 to produce the linear intermediate IM4 (Figure S4). IM4 undergoes further H migration and C−C bond fission via TS8 to produce propyne and CO (Figure S4). P3 results in three products, namely, H_2O, CO, and propyne, which lie 27.10 kcal/mol above the reactant (Figure 12).

All three products of path III were observed in the matrix-isolation FTIR spectra following the pyrolysis of oxolan-3-one. Carbon monoxide was assigned in Figure 3. Bands for propyne peaks were observed at 3323, 1446, and 629 cm^{-1} in Figures 4, 7, and 13 in accordance with published bands.[37,39−41] Care must be taken in assigning water as a pyrolysis product, as trace amounts of water are always present in a matrix-isolation FTIR spectrum due to unavoidable leaks in the vacuum chamber. For a definitive assignment, a comparison between the spectrum for heated oxolan-3-one and the spectrum for heated pure argon was needed. This comparison was done by integrating water bands from the two spectra, which were collected following identical deposition times and under similar laboratory conditions. The areas of both peaks of water shown in Figure 6 at 1624 and 1608 cm^{-1}, which match those in the literature,[20,42,43] were divided by the total amount of gas deposited, which was measured in Torr. The resultant-scaled areas were 0.005 and 0.003 for the peaks in the spectrum from oxolan-3-one pyrolysis and 0.002 and 0.001 for the peaks in the spectrum from heated argon. Therefore, the amount of water present in the spectrum of oxolan-3-one heated to 1400 K was over double that in the unheated spectrum, providing evidence for water being a product of thermal decomposition.

https://doi.org/10.1021/acs.jpca.2c03254
J. Phys. Chem. A 2022, 126, 7084−7093

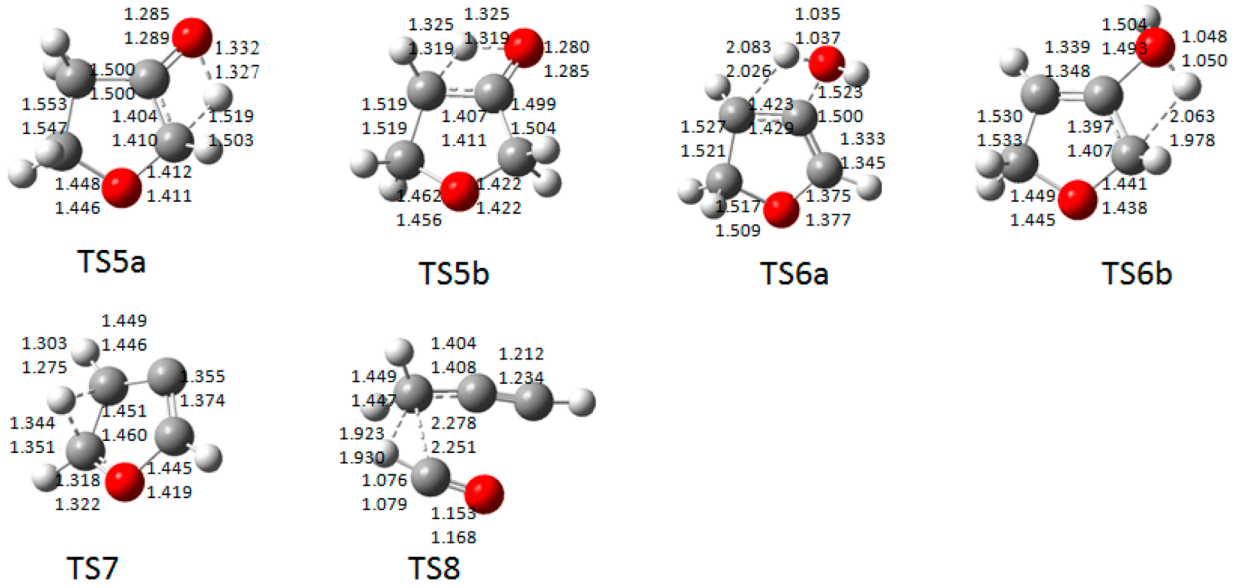

Figure 11. Optimized transition state geometries (Å) involved in path III (top, B3LYP/CBSB7; bottom, MP2/6-311++G**).

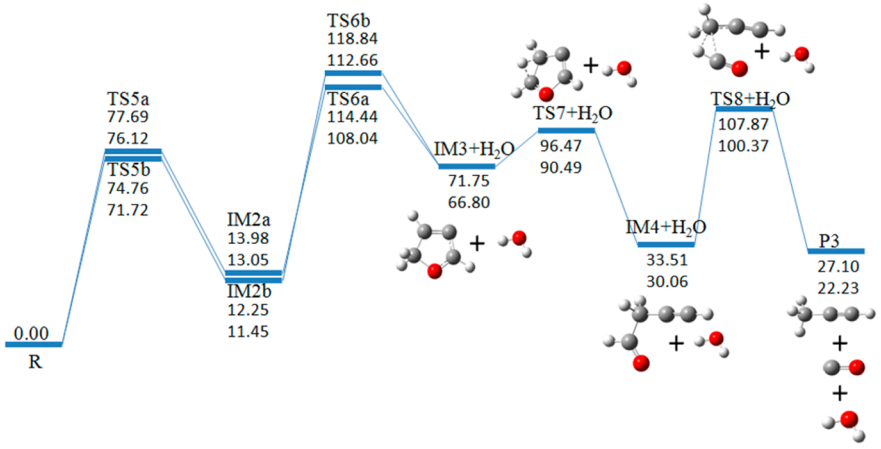

Figure 12. Relative energies (kcal/mol) of species involved in path III (up, CBS-QB3; down, G4MP2).

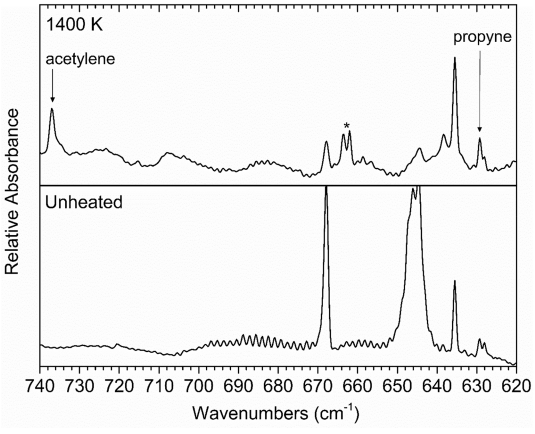

Figure 13. Comparison of the matrix infrared absorption spectrum collected after the pyrolysis of oxolan-3-one at 1400 K and the spectrum of the unheated sample. The propyne peak appears at 629 cm^{-1}. The bands centered at 663 cm^{-1} (*) belong to background CO_2.

D. PATH IV: THE PATHWAY FOR FORMATION OF P4 (R4), P5 (R5), P6 (R6), AND P7 (R7)

This pathway is initiated via two different types of hydrogen migration, with the simultaneous rupture of the ring via C−O bond fission. In the first case, a H atom migrates to the ring O atom from a C atom on either side. In the second case, a H atom shifts from one methylene to another, in addition to ring rupture caused by CO fission. Figure 14 shows the optimized transition states for path IV.

In the first case, a H atom migrates from either C2 or C10 via TS9 or TS11, respectively (Figure S5). The barriers for TS9 and TS11 range between 73 and 79 kcal/mol, respectively, which are comparable to the energetic barriers for TS5a and TS5b. TS9 leads to IM5 in which the O−C2 bond is broken, and IM5 further decomposes via concerted TS10, producing ethylene and hydroxyketene (R4). TS11 leads to a linear intermediate IM6 in which the O−C10 bond is broken. Further H migration from IM6 via TS12 leads to IM7, which undergoes a conformational interconversion to allow the formation of a four-membered-ring TS13 to produce acetylene + $HOCH_2CHO$ (R5). The relative energies of P4

https://doi.org/10.1021/acs.jpca.2c03254
J. Phys. Chem. A 2022, 126, 7084−7093

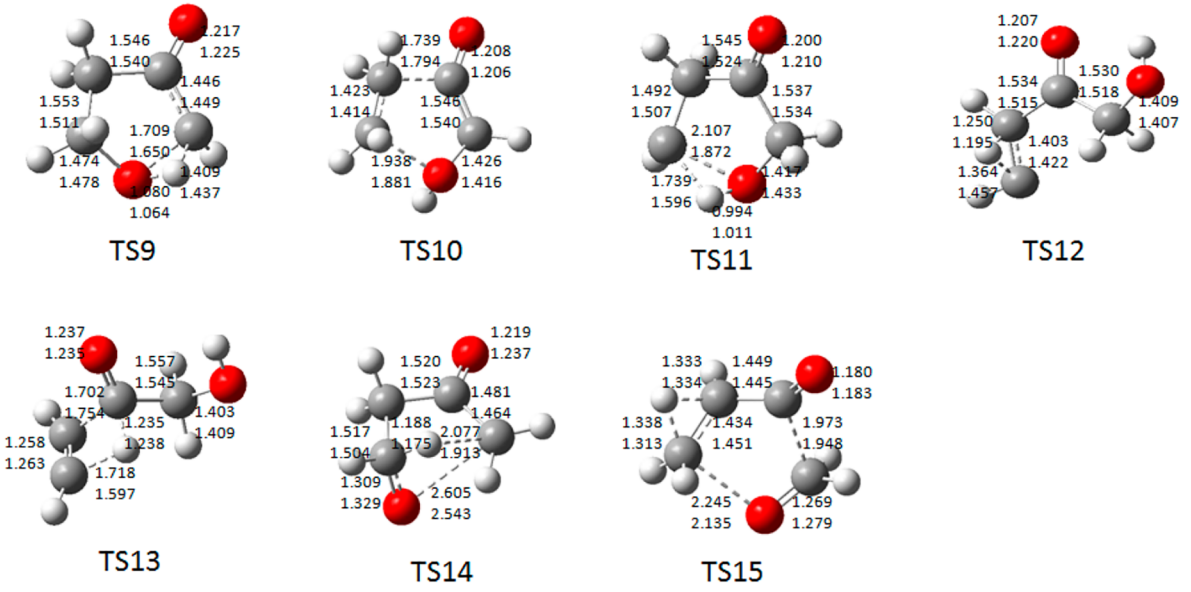

Figure 14. Optimized transition state geometries (Å) involved in path IV (top, B3LYP/CBSB7; bottom, MP2/6-311++G**).

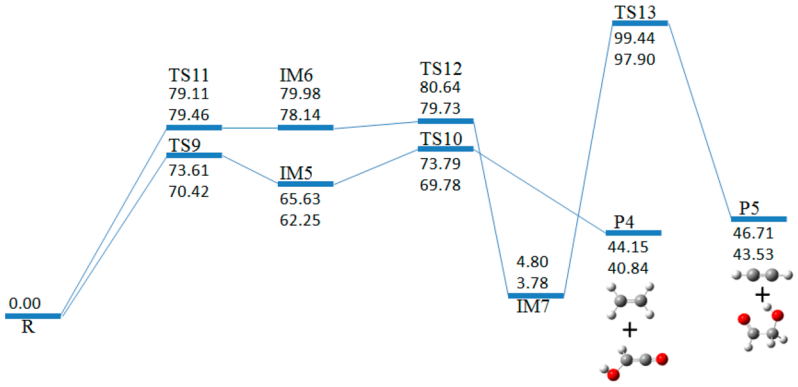

Figure 15. Relative energies (kcal/mol) of species involved in path IV H-migration to ring O with simultaneous CO fission (top, CBS-QB3; bottom, G4MP2).

and P5 are similar, ranging from 44.15 to 46.71 kcal/mol. Based on a comparison of their barrier heights, the production of P4 is more favorable than the production of P5 (Figure 15).

In the second case, we see H atom migration between methylene groups (Figure S6). For instance, in TS14, the H shifts across the ring from C10 to C2 and C−O fission occurs, leading to the linear product P6 (R6). This process is exothermic by 5.39 kcal/mol. In TS15, the H shifts from C10 to the adjacent C2, and the C−O and C−C bonds rupture simultaneously. TS15 leads to formaldehyde and methylketene P7 (R7). The production of P7 is endothermic by 25.63 kcal/mol, which is very close to the energetics associated with the production of P1. A comparison of the barrier heights for TS14 and TS15 suggests that the R6 channel is more favorable than the R7 channel (Figure 16).

There are many products associated with path IV, notably including two different substituted ketenes. The bands magnified in Figure 3 at 2125 and 2130 cm^{-1} cannot be assigned to ketene, carbon monoxide, or any clusters of those species and are very close to literature[33,36] bands and also those observed previously[41] at 2128 and 2124 cm^{-1} for methylketene in similar pyrolysis experiments performed on propionaldehyde using the same instrument. However, the

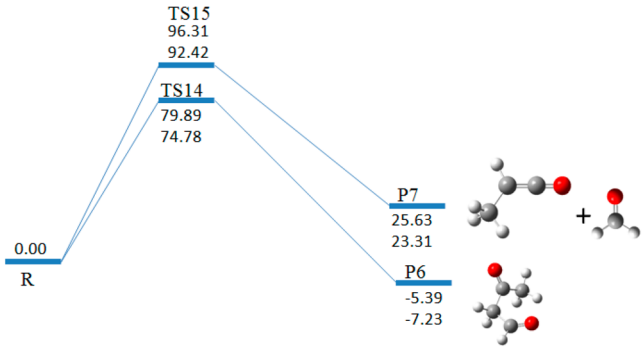

Figure 16. Relative energies (kcal/mol) of species involved in path IV H-migration between methylenes (top, CBS-QB3; bottom, G4MP2).

absorbance is very low ,and other methylketene bands at 1447, 1471, and 1075 cm^{-1} were not observed in these experiments on oxolan-3-one, so the assignment is tentative at best. The other substituted ketene in path IV, hydroxyketene, has no FTIR spectrum available in the literature. The C═C═O antisymmetric stretch of hydroxyketene was predicted to appear at 2131 cm^{-1} at the B3LYP/6-311G++(d,p) level of

https://doi.org/10.1021/acs.jpca.2c03254
J. Phys. Chem. A 2022, 126, 7084−7093

theory after being scaled by 0.964309, which is the (experimental/theoretical) scaling factor for ν_2 of ketene at the same level of theory; however, a difference of several wavenumbers between the calculated frequency and the experimental frequency could occur. In an attempt to generate and isolate hydroxyketene as an experimental benchmark, the pyrolysis of ethyl glycolate was performed prior to matrix isolation. (Figure S7) The pyrolysis of ethyl glycolate is hypothesized to produce hydroxyketene and ethanol, analogous to a scheme used to generate cyclopropylketene.[44] A band at 2140 cm^{-1} matches the band observed following oxolan-3-one pyrolysis in Figure 3. Again, this assignment is speculative, as the absorbance is low and there are no other prominent bands to confirm the assignment. The coproduct of hydroxyketene, ethylene, was detected in these experiments (*vide supra*) but was also associated with paths I and II.

It is noted that the activation free energy represents the driving power of reactions, which gives significant information on both the thermal equilibrium constants (K) and the rate constants (k) via

$$\Delta G_r = -RT\ln K \qquad k(T) = \frac{k_B T}{hc^0} e^{-\Delta G^{\neq}/RT}$$

where ΔG_r and $\Delta G^{\neq}$ represent the reaction Gibbs energy and the activation free energy, respectively. To demonstrate this, we also calculated the overall change in free energy for the main channel. $\Delta G^{\neq}$ and $\Delta H‡$ of TS1 were calculated to be 56.44 and 58.97 kcal/mol at the CBS-QB3 level, respectively; these values are very close to the value of ΔE that we used (57.86 kcal/mol). From these we can calculate that $T\Delta S^{\neq}$ is equal to 2.53 kcal/mol that and $\Delta S‡$ at 298.15 K is equal to 0.0085 kcal/mol·K, which indicates that the entropic factor for TS1 is relatively small. Therefore, it is feasible to estimate the magnitude of the activation energy using the transition state energy.

Except for simple C−H bond fission, we did not explore additional bond fission reactions leading to bimolecular or higher-order reactions, nor have we considered any possible roaming mechanisms. It has been established both experimentally[45] and theoretically[46] that bimolecular reactions can take place in these silicon carbide tubular reactors, especially at relatively high concentrations. While the scope of this work is limited to unimolecular pathways, the good agreement between our computational and experiments results provides a consistent picture of the initial decomposition pathways and sets the stage for a subsequent study exploring all possible bimolecular and higher order reactions.

It is worth noting that besides the singlet pathways discussed above, triplet products are also possible via simple C−C or C−O bond cleavage. However, the calculated heats of reaction are greater than 70 kcal/mol for C−C or C−O rupture (Supporting Information, Figure S8). Therefore, such direct C−C or C−O bond rupture processes are less likely than the singlet reactions described above. For completeness, we also calculated three different types of simple C−H rupture depending on the H sites. These C−H dissociation reactions lead to an H atom and the corresponding reactant radicals. Similar to simple C−C or C−O rupture, the processes for C−H rupture are also highly endothermic by more than 70 kcal/mol (Figure S8). Therefore, C−H bond rupture channels are not likely the main thermal decomposition mechanism.

CONCLUSIONS

Four distinct unimolecular decomposition pathways of oxolan-3-one have been discussed above. The most favorable pathway is path I, which has the lowest barrier (TS1) to produce the final products CO, CH_2O, and C_2H_4 (P1). The barrier heights for all the other pathways are more than 70 kcal/mol. In addition, except for pathway R6, all the channels are endothermic. P1, P2, P6, and P7 could be generated in one step, while the others need more than one step. Therefore, the pyrolysis of oxolan-3-one has one dominant product channel, namely, the formation of CO, CH_2O, and C_2H_4 via R1. Moreover, most of the pyrolysis products have been observed experimentally, such as carbon monoxide, formaldehyde, ethylene, ketene, acetylene, propyne, and water. While there is some evidence suggesting hydroxyketene and methylketene as minor products, additional experiments are needed to confirm the assignments or to identify other products, for instance, products from P6.

ASSOCIATED CONTENT

Supporting Information

The Supporting Information is available free of charge at https://pubs.acs.org/doi/10.1021/acs.jpca.2c03254.

Cartesian coordinates for all B3LYP/CBSB7-optimized structures, optimized geometries for paths II−IV, and the FTIR spectrum suspected to show hydroxyketene (PDF)

AUTHOR INFORMATION

Corresponding Authors

Laura R. McCunn − *Department of Chemistry, Marshall University, Huntington, West Virginia 25755, United States;* orcid.org/0000-0003-4877-5553; Email: mccunn@marshall.edu

Xinli Song − *Wuhan Institute of Physics and Mathematics, Innovation Academy for Precision Measurement Science and Technology, Chinese Academy of Sciences, Wuhan, Hubei 430071, China*; Email: xinli.song@apm.ac.cn

Authors

Heather N. Legg − *Department of Chemistry, Marshall University, Huntington, West Virginia 25755, United States*

Kathryn M. Narkin − *Department of Chemistry, Marshall University, Huntington, West Virginia 25755, United States*

Carol A. Parish − *Department of Chemistry, University of Richmond Gottwald Center for the Sciences, Richmond, Virginia 23173, United States;* orcid.org/0000-0003-2878-3070

Complete contact information is available at: https://pubs.acs.org/10.1021/acs.jpca.2c03254

Notes

The authors declare no competing financial interest.

ACKNOWLEDGMENTS

The experimental results are based on work supported by the U.S. Department of Energy, Office of Science under Award DE-SC0019732. The authors acknowledge Barney Ellison for helpful insight into the pyrolytic generation of ketenes. H.N.L. acknowledges a William C. Dudley Summer Undergraduate Research Fellowship, the Lacy Stone Memorial Chemistry Scholarship, and the Daniel Babb Trust. L.R.M. acknowledges

a Marshall University Summer Research Award. C.A.P. acknowledges funding from the National Science Foundation (Grant CHE-18800014), the Donors of the American Chemical Society Petroleum Research Fund, and the Floyd D. and Elisabeth S. Gottwald Endowment. X.S. acknowledges that this work was supported by the National Natural Science Foundation of China (no. 21503270)

REFERENCES

(1) Liu, W.-J.; Li, W.-W.; Jiang, H.; Yu, H.-Q. Fates of Chemical Elements in Biomass During Its Pyrolysis. *Chem. Rev.* **2017**, *117*, 6367−6398.
(2) Vamvuka, D. Bio-Oil, Solid and Gaseous Biofuels from Biomass Pyrolysis Processes—an Overview. *Int. J. Energy Res.* **2011**, *35*, 835−862.
(3) Anca-Couce, A. Reaction Mechanisms and Multi-Scale Modelling of Lignocellulosic Biomass Pyrolysis. *Prog. Energy Combust. Sci.* **2016**, *53*, 41−79.
(4) Nanda, S.; Mohammad, J.; Reddy, S. N.; Kozinski, J. A.; Dalai, A. K. Pathways of Lignocellulosic Biomass Conversion to Renewable Fuels. *Biomass Convers. Biorefin* **2014**, *4*, 157−191.
(5) Charon, N.; Ponthus, J.; Espinat, D.; Broust, F.; Volle, G.; Valette, J.; Meier, D. Multi-Technique Characterization of Fast Pyrolysis Oils. *J. Anal. Appl. Pyrolysis* **2015**, *116*, 18−26.
(6) Kanaujia, P. K.; Sharma, Y. K.; Agrawal, U. C.; Garg, M. O. Analytical Approaches to Characterizing Pyrolysis Oil from Biomass. *TrAC, Trends Anal. Chem.* **2013**, *42*, 125−136.
(7) Stas, M.; Kubicka, D.; Chudoba, J.; Pospisil, M. Overview of Analytical Methods Used for Chemical Characterization of Pyrolysis Bio-Oil. *Energy Fuels* **2014**, *28*, 385−402.
(8) Oasmaa, A.; Kuoppala, E.; Solantausta, Y. Fast Pyrolysis of Forestry Residue. 2. Physicochemical Composition of Product Liquid. *Energy Fuels* **2003**, *17*, 433−443.
(9) Fendt, A.; Geissler, R.; Streibel, T.; Sklorz, M.; Zimmermann, R. Hyphenation of Two Simultaneously Employed Soft Photo Ionization Mass Spectrometers with Thermal Analysis of Biomass and Biochar. *Thermochim. Acta* **2013**, *551*, 155−163.
(10) Galletti, G. C.; Chiavari, G.; Kahie, Y. D. Pyrolysis/Gas Chromatography/Ion-Trap Mass Spectrometry of the 'Tooth Brush' Tree (Salvadora Persica L.). *Rapid Commun. Mass Spectrom.* **1993**, *7*, 651−655.
(11) Mulder, M. M.; Pureveen, J. B. M.; Boon, J. J.; Martinez, A. T. An Analytical Pyrolysis Mass Spectrometric Study of Eucryphia Cordifolia Wood Decayed by White-Rot and Brown-Rot Fungi. *J. Anal. Appl. Pyrolysis* **1991**, *19*, 175−191.
(12) Zhang, X.; Friderichsen, A. V.; Nandi, S.; Ellison, G. B.; David, D. E.; McKinnon, J. T.; Lindeman, T. G.; Dayton, D. C.; Nimlos, M. R. Intense, Hyperthermal Source of Organic Radicals for Matrix-Isolation Spectroscopy. *Rev. Sci. Instrum.* **2003**, *74*, 3077−3086.
(13) Frisch, M. J.; Trucks, G. W.; Schlegel, H. B.; Scuseria, G. E.; Robb, M. A.; Cheeseman, J. R.; Scalmani, G.; Barone, V.; Mennucci, B.; Petersson, G. A.et al.*Gaussian 16*, rev. A.02; Gaussian, Inc.: Wallingford, CT, 2016.
(14) Becke, A. D. Density-Functional Thermochemistry. III. The Role of Exact Exchange. *J. Chem. Phys.* **1993**, *98*, 5648−5652.
(15) Gonzalez, C.; Schlegel, H. B. An Improved Algorithm for Reaction Path Following. *J. Chem. Phys.* **1989**, *90*, 2154−2161.
(16) Montgomery, J. A.; Frisch, M. J.; Ochterski, J. W.; Petersson, G. A. A Complete Basis Set Model Chemistry. Vi. Use of Density Functional Geometries and Frequencies. *J. Chem. Phys.* **1999**, *110*, 2822−2827.
(17) Curtiss, L. A.; Redfern, P. C.; Raghavachari, K. Gaussian-4 Theory Using Reduced Order Perturbation Theory. *J. Chem. Phys.* **2007**, *127*, 124105.
(18) Song, X.; Parish, C. A. Pyrolysis Mechanisms of Thiophene and Methylthiophene in Asphaltenes. *J. Phys. Chem. A* **2011**, *115*, 2882−2891.
(19) Song, X.; Fanelli, M. G.; Cook, J. M.; Bai, F.; Parish, C. A. Mechanisms for the Reaction of Thiophene and Methylthiophene with Singlet and Triplet Molecular Oxygen. *J. Phys. Chem. A* **2012**, *116*, 4934−4946.
(20) Givan, A.; Loewenschuss, A.; Nielsen, C. J. FTIR Studies of CO-Water Complexes in Argon Matrixes and in Porous Ices. *J. Chem. Soc., Faraday Trans* **1996**, *92*, 4927−4933.
(21) Abe, H.; Takeo, H.; Yamada, K. M. T. Infrared Spectroscopy of CO Trapped in an Argon Matrix Revisited. *Chem. Phys. Lett.* **1999**, *311*, 153−158.
(22) Abe, H.; Yamada, K. M. T. Infrared Spectra of the CO−H2o 1−1 Cluster Trapped in an Argon Matrix. *J. Chem. Phys.* **2001**, *114*, 6134−6141.
(23) Abe, H.; Yamada, K. M. T. Spectroscopic Identification of the CO-H2o 2−1 Cluster Trapped in an Argon Matrix. *J. Chem. Phys.* **2004**, *121*, 7803−7812.
(24) McNally, D.; Ault, B. S. Infrared Matrix Isolation Study of the Thermal and Photochemical Reactions of Ozone with Dimethylcadmium. *J. Phys. Chem. A* **2012**, *116*, 1914−1922.
(25) Khoshkhoo, H.; Nixon, E. R. Infrared and Raman Spectra of Formaldehyde in Argon and Nitrogen Matrices. *Spectrochim. Acta, Part A* **1973**, *29*, 603−612.
(26) Thompson, M. G. K.; Parnis, J. M. FTIR Analysis of Dimethyl Ether Decomposition Products Following Charge Transfer Ionization with Ar^+ under Matrix Isolation Conditions. *J. Phys. Chem. A* **2008**, *112*, 12109−12116.
(27) Harvey, K. B.; Ogilvie, J. F. Infrared Absorption of Formaldehyde at Low Temperatures: Evidence for Multiple Trapping Sites in an Argon Matrix. *Can. J. Chem.* **1962**, *40*, 85−91.
(28) Barnes, A. J.; Howells, J. D. R. Infra-Red Cryogenic Studies. Part 12.-Alkenes in Argon Matrices. *J. Chem. Soc., Faraday Trans. 2* **1973**, *69*, 532−539.
(29) Thompson, M. G. K.; Parnis, J. M. Photoinduced Ethane Formation from Reaction of Ethene with Matrix-Isolated Ti, V, or Nb Atoms. *J. Phys. Chem. A* **2005**, *109*, 9465−9470.
(30) Kafafi, Z. H.; Hauge, R. H.; Margrave, J. L. Photochemistry of Iron Atoms and Dimers with Ethylene in Cryogenic Matrixes. The FT-IR Spectrum of Ethenyliron Hydride. *J. Am. Chem. Soc.* **1985**, *107*, 7550−7559.
(31) Vasiliou, A. K.; Piech, K. M.; Reed, B.; Zhang, X.; Nimlos, M. R.; Ahmed, M.; Golan, A.; Kostko, O.; Osborn, D. L.; David, D. E.; et al. Thermal Decomposition of CH_3CHO Studied by Matrix Infrared Spectroscopy and Photoionization Mass Spectroscopy. *J. Chem. Phys.* **2012**, *137*, 164308.
(32) Moore, C. B.; Pimentel, G. C. Infrared Spectrum and Vibrational Potential Function of Ketene and the Deuterated Ketenes. *J. Chem. Phys.* **1963**, *38*, 2816−2829.
(33) Winter, P. R.; Rowland, B.; Hess, W. P.; Radziszewski, J. G.; Nimlos, M. R.; Ellison, G. B. UV Photodissociation of Matrix-Isolated Propionyl Chloride. *J. Phys. Chem. A* **1998**, *102*, 3238−3248.
(34) Vasiliou, A.; Piech, K. M.; Zhang, X.; Nimlos, M. R.; Ahmed, M.; Golan, A.; Kostko, O.; Osborn, D. L.; Daily, J. W.; Stanton, J. F.; et al. The Products of the Thermal Decomposition of CH_3CHO. *J. Chem. Phys.* **2011**, *135*, 014306.
(35) Kline, E. S.; Kafafi, Z. H.; Hauge, R. H.; Margrave, J. L. Matrix-Isolation Studies of the Reactions of Iron Atoms and Iron Dimers with Acetylene in an Argon Matrix. The FT-IR Spectrum of Ethynyliron Hydride. *J. Am. Chem. Soc.* **1985**, *107*, 7559−7562.
(36) Harrison, J. A.; Frei, H. Visible Light-Induced Oxygen Transfer from Nitrogen Dioxide to Ethyne and Propyne in a Cryogenic Matrix. 1. Identification of Products. *J. Phys. Chem.* **1994**, *98*, 12142−12151.
(37) Andrews, L. FTIR Spectra of Hydrogen Fluoride Complexes in Solid Argon. *J. Phys. Chem.* **1984**, *88*, 2940−2949.
(38) Wright, E. M.; Warner, B. J.; Foreman, H. E.; McCunn, L. R.; Urness, K. N. Pyrolysis Reactions of 3-Oxetanone. *J. Phys. Chem. A* **2015**, *119*, 7966−7972.
(39) Araujo-Andrade, C.; Gomez-Zavaglia, A.; Reva, I. D.; Fausto, R. Conformers, Infrared Spectrum and UV-Induced Photochemistry of

https://doi.org/10.1021/acs.jpca.2c03254
J. Phys. Chem. A 2022, 126, 7084−7093

Matrix-Isolated Furfuryl Alcohol. *J. Phys. Chem. A* **2012**, *116*, 2352−2365.
(40) Sias, E. R.; Cole, S. L.; Warner, B. J.; Wright, E. M.; McCunn, L. R. The Effect of Aldehyde Structure on Pyrolysis Reactions. *J. Anal. Appl. Pyrolysis* **2017**, *123*, 340−346.
(41) Warner, B. J.; Wright, E. M.; Foreman, H. E.; Wellman, C. D.; McCunn, L. R. Products from Pyrolysis of Gas-Phase Propionaldehyde. *J. Phys. Chem. A* **2015**, *119*, 14−23.
(42) Redington, R. L.; Milligan, D. E. Infrared Spectroscopic Evidence for the Rotation of the Water Molecule in Solid Argon. *J. Chem. Phys.* **1962**, *37*, 2162−2166.
(43) Bentwood, R. M.; Barnes, A. J.; Orville-Thomas, W. J. Studies of Intermolecular Interactions by Matrix Isolation Vibrational Spectroscopy: Self-Association of Water. *J. Mol. Spectrosc.* **1980**, *84*, 391−404.
(44) Berkowitz, W. F.; Ozorio, A. A. Pyrolyses of Cyclopropylketene Dimer and Ethyl Cyclopropaneacetate. *J. Org. Chem.* **1975**, *40*, 527−528.
(45) Couch, D. E.; Buckingham, G. T.; Baraban, J. H.; Porterfield, J. P.; Wooldridge, L. A.; Ellison, G. B.; Kapteyn, H. C.; Murnane, M. M.; Peters, W. K. Tabletop Femtosecond VUV Photoionization and Pepico Detection of Microreactor Pyrolysis Products. *J. Phys. Chem. A* **2017**, *121*, 5280−5289.
(46) Sivaramakrishnan, R.; Michael, J. V.; Harding, L. B.; Klippenstein, S. J. Resolving Some Paradoxes in the Thermal Decomposition Mechanism of Acetaldehyde. *J. Phys. Chem. A* **2015**, *119*, 7724−7733.

https://doi.org/10.1021/acs.jpca.2c03254
J. Phys. Chem. A 2022, 126, 7084−7093